Chapter 3

XSL carbon star spectra between 0.4 and 2.4 μm: comparison with models [1]

⋆ ⋆ ⋆

A. Gonneau, A. Lançon, S. C. Trager, B. Aringer, W. Nowotny

To be submitted to Astronomy & Astrophysics

Abstract

We make use of a collection of carbon star spectra, obtained as part of the X-shooter Spectral Library, to infer some carbon-rich models. The observed spectra span from 0.4 to 2.4 μm and present quite a variety in $(J - K)$, chemical enrichment and pulsation properties. Because of the bimodal behaviour of our sample, highlighted by the presence of an absorption band at 1.53 μm, the comparison with the hydrostatic models is not straightforward.

[1] Based on observations collected at the European Southern Observatory, Paranal, Chile, Prog. ID 084.B-0869(A/B), 085.B-0751(A/B), 189.B-0925(A/B/C/D).

3.1 Introduction

Modelling the spectra of luminous red stars, such as red supergiants or luminous asymptotic giant branch stars, remains an immense challenge. These stars have hugely extended atmospheres which host molecules and sometimes dust. Their heavy element abundance ratios are non-solar as the result of dredge-up episodes in their previous evolutionary history. This is particularly true for carbon stars (C stars), whose atmospheres have carbon-to-oxygen abundance ratios larger than 1. Many, if not all, luminous red stars are variable due to pulsation (Wood 2015), and pulsation sends shock waves through the atmospheres. In addition, interferometric observations have demonstrated significant departures from spherical symmetry in some of these objects, that have been interpreted as the signatures of large scale convective cells. In the case of red supergiants, these inhomogeneities have been identified as a plausible cause of differences between the stellar effective temperatures estimated from optical molecular bands on one hand, or from the spectral energy distribution on the other (Davies et al. 2013). Qualitatively similar inhomogeneities have been discovered in asymptotic giant branch stars (van Belle et al. 2013).

However, luminous red stars can be observed at very large distances, and they contribute significantly to the light of certain galaxies especially at red and near-infrared (NIR) wavelengths. Their relative numbers are predicted to be sensitive functions of age and initial metallicity. Their importance in studies of the stellar populations of local and remote galaxies justifies the continuous efforts devoted both to their empirical characterization and to their modelling.

In a previous article (Gonneau et al. 2015, hereafter *Chapter 2*), we have described new spectroscopic observations of carbon stars (C stars) obtained with the ESO/VLT/X-shooter instrument as part of the XSL project (X-shooter Spectral Library, PI. S. C. Trager). This collection is the first to provide simultaneous optical and NIR observations at a resolving power $R = \lambda/\delta\lambda \sim 8000$. Hence it offers a unique possibility to test state-of-the art synthetic spectra of C stars. For stars that can be reproduced in a satisfactory fashion, estimates of the stellar fundamental parameters may be derived. These estimates are essential if the empirical spectra are to be used as templates in future studies of the stellar populations of galaxies.

A recent series of four articles has provided the largest current collection of model atmospheres and low-resolution theoretical spectra for C stars (Aringer et al. (2009), Nowotny et al. (2011, 2013), Eriksson et al. (2014) – respectively referred to as Papers T1 to T4 hereafter). These papers demonstrate that only the energy distributions of relatively blue asymptotic giant branch C stars (in that case, $J-K \leq 1.5$) can be matched with hydrostatic models. The energy distributions of redder objects result from the combination of photospheric emission and radiative transfer through the dusty circumstellar material, that is produced naturally as a result of pulsation. The dynamic models of these series are able to reproduce the location of C stars in a number of color-magnitude and color-color diagrams, and also reproduce typical properties of the mass loss and wind velocities.

In this article, we focus on the hydrostatic models of T1. Early synthetic spectra based on these models were used by Paladini et al. (2011) to analyse low-resolution spectra ($400 < R < 1800$) of C stars with no circumstellar dust in the near-infrared ($0.9 < \lambda < 4.2\,\mu$m), together with interferometric observations. It allowed the authors to select prefered line lists for C_2. They concluded that the C_2H_2 feature at $3.1\,\mu$m was the spectral signature most sensitive to effective temperature. A large grid of new high-resolution theoretical spectra based on the hydrostatic models of T1 has been computed for the present article. High-resolution theoretical spectra for the pulsating models of T2, T3, T4 are not yet available. The following questions guide our comparisons with the X-shooter observations. Can the optical-to-near infrared spectra be matched reasonably well, for stars with little or no evidence of circumstellar dust? To what extent are parameters estimated from optical wavelengths compatible with those obtained from NIR wavelengths?

The paper is organized as follows. Section 3.2 describes the input carbon-rich spectra and Section 3.3 presents the theoretical grid of models. Section 3.4 shows the first part of the study: a comparison between models. In Section 3.5, we use the result from Section 3.4 and compare our observations with the previous models. In Section 3.6, we discuss the results and conclude the paper.

3.2 Observations

Our sample of carbon stars is composed of 35 medium-resolution spectra, observed with the European Southern Observatory (ESO/VLT) spectrograph X-shooter (Vernet et al. 2011). The beauty of this instrument lies in the fact that it allows simultaneous acquisition of spectra from 0.3 to $2.5\,\mu$m, using two dichroics to split the beam into three arms, respectively ultraviolet-blue (UVB), visible (VIS), and near-infrared (NIR).

The C-star spectra were acquired as part of the X-shooter Spectral Library (hereafter XSL, Chen et al. 2014a), through an ESO Large Programme. This empirical library contains about 700 stars, observed at a moderate resolving power ($7\,700 \leq R \leq 11\,000$ depending on the arm) and covering a large range of stellar atmospheric parameters.

Our sample of carbon stars includes stars from the Milky Way (MW) and the Large and Small Magellanic Clouds (LMC, SMC). Details about the star selection and the data reduction can be found in *Chapter 2* Here, we only briefly recall the properties of the resulting spectra.

Our sample presents quite a diversity in spectral shape and absorption-line characteristics. The highlight of our previous paper was a bimodal behaviour among carbon stars with relatively red near-infrared colors. Some of our carbon stars with $(J - K) > 1.6$ display an absorption band at $1.53\,\mu$m, which is usually associated to HCN+C_2H_2 (Gautschy-Loidl et al. 2004). In our sample, the $1.53\,\mu$m feature was also associated to a smoother near-infrared spectrum and an energy distribution with two components, one peaking at red optical wavelengths, the other at long wavelengths.

In the following, our sample will be divided in four groups, which can be different from the groups described in *Chapter 2*. The first group (A) will gather the bluest C stars from our sample, with $(J-K) < 1.2$. It remains the same as Group 1. The second group (B) will gather the classical C stars with $1.2 < (J-K) < 1.6$, as Group 2. The two last groups will gather all the carbon stars with $(J-K) > 1.6$. The dichotomy between the stars displaying or not the 1.53 μm absorption will be used to separate the stars into two groups. The stars from the former Groups 3 and 4 without this absorption feature will be in Group C. All the other stars, thus with the absorption feature, will be gathered in Group D.

Name	Galaxy	$(J-K_s)$ [mag]	Gr. I	Gr. II
HD 202851	MW	0.65	1	A
HE 1428-1950	MW	0.72	1	A
Cl* NGC 121 T V8	SMC	0.95	1	A
SHV 0518161-683543	LMC	0.98	1	A
SHV 0517337-725738	LMC	1.09	1	A
2MASS J00571648-7310527	SMC	1.28	2	B
2MASS J00563906-7304529	SMC	1.29	2	B
2MASS J01003150-7307237	SMC	1.32	2	B
2MASS J00530765-7307477	SMC	1.35	2	B
2MASS J00493262-7317523	SMC	1.39	2	B
2MASS J00490032-7322238	SMC	1.43	2	B
2MASS J00571214-7307045	SMC	1.47	2	B
2MASS J00570070-7307505	SMC	1.58	2	B
2MASS J00564478-7314347	SMC	1.69	3	C
2MASS J00542265-7301057	SMC	1.81	3	C
IRAS 09484-6242	MW	1.84	3	C
Cl* NGC 419 LE 27	SMC	1.92	3	C
[W65] c2	MW	1.94	3	C
SHV 0520427-693637	LMC	1.94	3	C
2MASS J00553091-7310186	SMC	2.02	3	C
Cl* NGC 419 LE 35	SMC	2.04	3	C
SHV 0504353-712622	LMC	2.09	3	C
T Cae	MW	2.19	3	C
[ABC89] Cir 18	MW	2.41	4	C
[ABC89] Pup 42	MW	2.66	4	C
[ABC89] Cir 18	MW	2.74	4	C
SHV 0500412-684054	LMC	1.84	3	D
SHV 0502469-692418	LMC	1.99	3	D
SHV 0527072-701238	LMC	2.32	4	D
SHV 0520505-705019	LMC	2.40	4	D
SHV 0518222-750327	LMC	2.50	4	D
SHV 0536139-701604	LMC	2.96	4	D
SHV 0525478-690944	LMC	3.05	4	D
SHV 0528537-695119	LMC	3.16	4	D

Table 3.1: Main properties of our observed carbon stars

Table 3.1 lists the observed carbon stars used in this paper. All spectra are plotted in the appendix of *Chapter 2*. In the following, we will not discuss the case of V CrA, a star of type R Coronae Borealis (R CrB) that was undergoing an obscuration event at the time of observation. Its spectrum is dominated by circumstellar emission and shows no photospheric features.

3.3 Carbon-rich hydrostatic models

We use a grid of theoretical models atmospheres computed specifically for this project, in the framework of Aringer et al. (2009). These models are hydrostatic dust-free carbon-rich models, based on spherically symmetric COMARCS atmospheres.

3.3.1 Initial grid

The original series of models covers a wide range of parameters in effective temperatures, surface gravities and carbon over oxygen ratios. In addition, sub-grids with various metallicities were computed, in order to reproduce the population from the Milky Way and the Magellanic Clouds, and also various masses.

For the microturbulent velocity, a value of $\xi = 2.5$ km s^{-1} was adopted. The models were calculated in the range $\tau_{Rosseland} = 10^2$ to 10^{-5} with a constant logarithmic step size of 0.1.

The hydrostatic COMARCS atmospheres were then used to compute synthetic opa-city sampling spectra covering the range between 0.444 to 25.0 μm with a resolution of R = 10000. Due to the statistical nature of the opacity sampling, only the average over a large number of wavelength points (usually 20 to 100) gives a realistic representation of the observed stellar spectra. Thus, the resolution was reduced to R = 200 by convolving their spectra with a Gaussian function defined by the corresponding half width. No additional broadening caused for example by a macroturbulent velocity was assumed.

3.3.2 New grid

Due to the resolution of the X-shooter spectra ($\simeq$ 10000), the actual resolution of the models was not sufficient to perform high resolution comparisons. A new grid of models was computed with a resolution of R = 200000, that we smoothed afterwards to match the resolution of our spectra. These models were computed for solar abundances and for M = 1.0 $M_{\odot}$. The effective temperature of the models spans from 2500 to 4000 K, with a step of 100 K. The surface gravity takes the following values: -0.4, 0 and 2. The ratio of carbon over oxygen is sampled as follows: 1.01, 1.05, 1.10, 1.40 and 2.0. A second set of models with $[Fe/H] = -0.5$ was also computed. Figure 3.1 shows a schematic representation of all the models available, as a function of the parameters listed before.

It is important to keep in mind that although this grid is a good starting point, it does not vary all the relevant parameters. We know from red supergiants that at least the turbulent velocity parameters and the nitrogen abundance will affect the relative strengths of molecular bands.

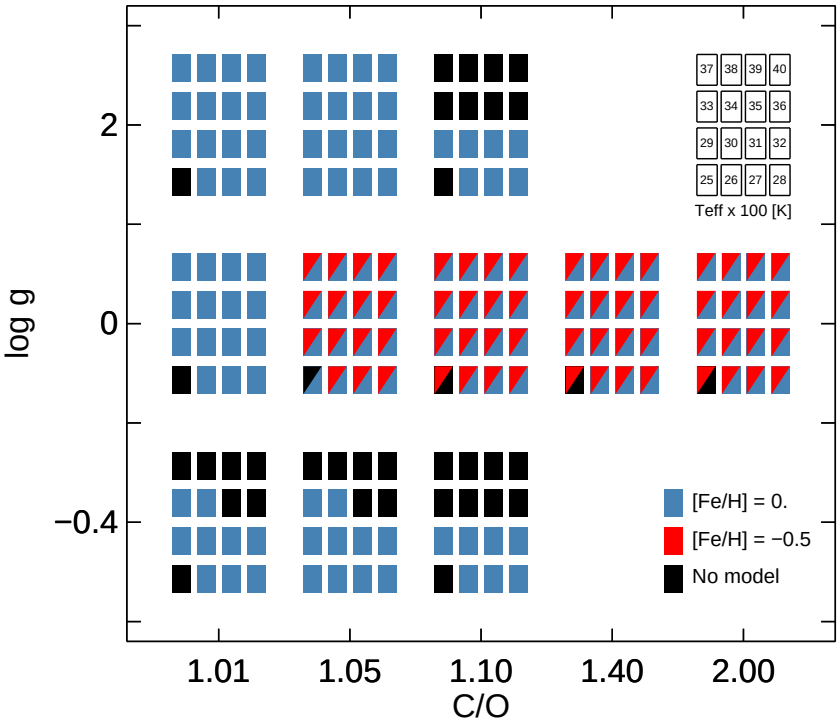

Figure 3.1: Schematic overview showing our grid of models.

3.3.3 Examples of model spectra

Figure 3.2 shows an example of a model spectrum at high resolution (R = 200000) as a black curve and its smoothed version (R $\simeq$ 10000) as a red curve. The parameters of the model used are listed on the top-right corner of the figure. By smoothing the high resolution model spectra we loose the information of the continuum.

Figure 3.3 shows three hydrostatic models which share the same properties except the temperature. The temperature decreases from the top to the bottom. The peak of the SED slowly shifts from the blue to the red, when the spectra get cooler. The strongest bandheads and the ragged aspect of the spectra are due mostly to numerous lines from CN and C_2, which tend to increase with decreasing temperature. The signatures with a weaker dependence on T_{eff} over the plotted range, such as those of CO around 1.65 and 2.3 μ, are progressively masked into a forest of other features when T_{eff} decreases.

The effects of the fundamental parameters on the spectra are not obvious to the eye in plots of the whole spectrum. They are more efficiently summarized by index measurements, as shown below.

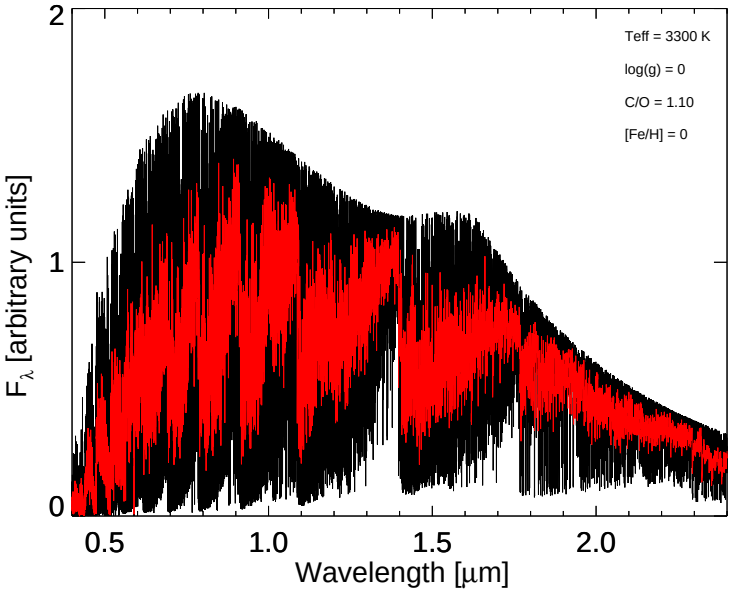

Figure 3.2: Example of a model spectrum at high resolution (black curve) and smoothed to XSL resolution (red curve).

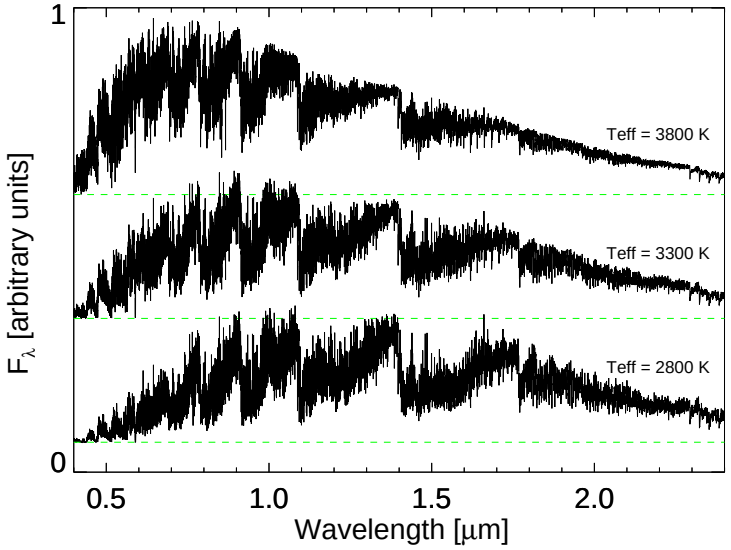

Figure 3.3: Examples of synthetic spectra of C-rich giants with different temperatures ($\log(g)$ =0, C/O = 1.10 and [Fe/H] = 0). The spectra are normalized around 1.35 μm for display purposes.

3.3.4 Molecular indices of model spectra

In *Chapter 2*, we defined spectroscopic indices for carbon stars. We calculated the values of these indices for the grid of models. We define a new version of the index $DIP153$, based on the clear separation, shown in *Chapter 2*, between the stars with and without the 1.53 μm absorption feature. To do so, we fit the averaged values of the $DIP153$ index (as a function of $(J - K_S)$) for our (observed) stars without the 1.53 μm feature, and subtract these values to the values of the $DIP153$ index.

$$DIP153b = DIP153 - \text{fit} = DIP153 - 0.123 * (1 - (J - K_S)) \qquad (3.1)$$

Figure 3.4 shows the values of four representative near-infrared indices as a function of the effective temperature of the models. In addition to $DIP153b$, we plot CN, which measures the strength of the CN molecule at 1.11 μm, $C2$, which measures the bandhead of the C_2 molecule at 1.77 μm, and $CO12$, which measures the first overtone ro-vibrational band of CO at 2.3 μm. The symbol sizes represent model C/O ratios in the upper panels, model surface gravities in the lower panels.

As a general trend, molecular bandhead strengths increase with decreasing temperatures. This is the case for CN, C_2 and CO. At the lowest temperatures, contamination of the index passbands by lines from other molecules (or other bands of the same molecule) weakens the index values.

At a given T_{eff}, the bands of CN and C_2 increase with C/O, while CO decreases. For the surface gravity, the strengths of the bands increase with decreasing $\log(g)$. For $T_{eff} < 3000$ K, the high-gravity models ($\log(g)$=2) really contrast with the other models.

From the plots showing $DIP153b$ versus temperature, it is clear that some of the cool models ($T_{eff} < 3000$ K) display the 1.53 μm absorption band.

3.4 Comparison of pseudo-observations and models

3.4.1 Study of pseudo-observations

Before comparing our observations to the grid of models, it is important to evaluate the amount of information present in the models themselves. If the models were perfect representations of the reality, with what uncertainties could we estimate the values of the fundamental parameters, such as T_{eff}, $\log(g)$, C/O? To answer that question, we select a subset of models that we analyse with the full model grid as if they were observations. We refer to the subset as pseudo-observations. Table 3.2 summarizes the parameters of the pseudo-observations.

Before analysis, the pseudo-observations are smoothed to a resolving power comparable to X-shooter spectra, R $\sim$ 10000 and resampled. Artificial gaussian noise is added, to reach a signal-to-noise ratio of 75 per pixel. Because these models are hydrostatic and thus dust-free, we redden them artificially with A_V = 1, using the extinction law of Cardelli et al. (1989).

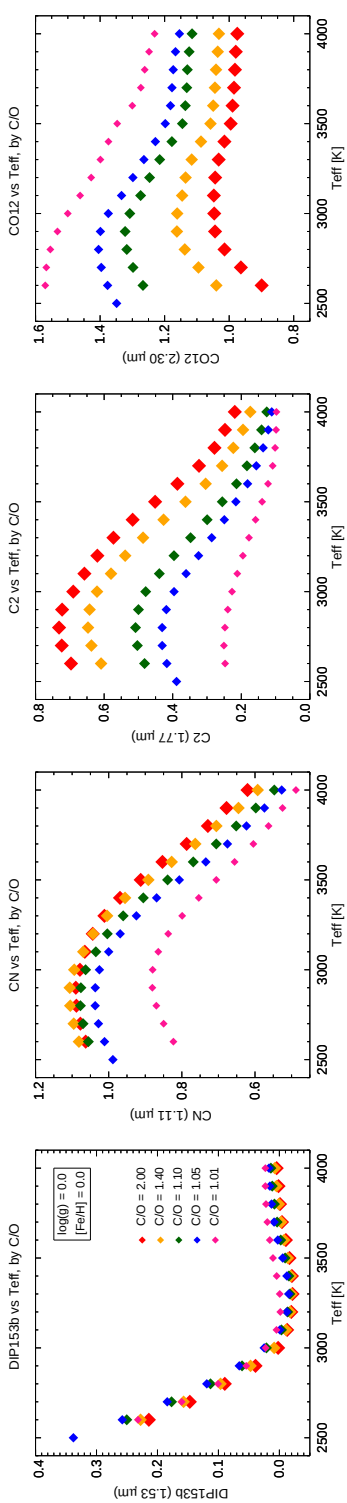

Figure 3.4: Molecular indices vs T_{eff} for a representative set of models. The symbols are for C/O in the upper panels and for $\log(g)$ in the lower panels. More indices are shown in Fig. 3.8.

Input parameters	Values
T_{eff} [K]	2600 - 3300 - 3800
$\log(g$ [cm/s^2])	0.0
C/O	1.05 - 1.40
[Fe/H]	0.0
A_V	1

Table 3.2: Properties of the subset of models selected as pseudo-observations

3.4.2 Methodology

To compare our pseudo-observations to the models, we perform a χ^2 minimization in a four-dimensional space. The grid of models spans four dimensions which are T_{eff}, $\log(g)$, (C/O) and [Fe/H].

To absorb any residual flux calibration errors in the observed data, a multiplicative spline polynomial is used instead of a standard extinction law to reshape the energy distribution. For consistency, it is important to note that this can only mimic multiplicative effects of circumstellar dust such as extinction, and not additive effects such as any continuous emission by dust.

In order to avoid unphysical dereddening of the models, we exclude any models intrinsically redder than the fitted observed spectrum, based on $(R-I)$ for the UVB/VIS range or $(J-K)$ for the NIR. A tolerance of 10% on these colors is implemented as an allowance for spectrophotometric errors in the data.

The reduced χ^2 is calculated as follows:

$$\chi^2_{red} = \frac{1}{N}\sum_{i=1}^{M} W(i) \times \frac{(F_{obs}(i) - polynomial \times F_{mod}(i))^2}{\sigma^2_{F_{obs}}(i)}, \tag{3.2}$$

with: F the observed or theoretical flux, σ the noise spectrum of the observation and W the weights assigned to each pixel. The weights take values of 0 in the regions of strong telluric absorption[2], and 1 elsewhere. M is the total number of pixels and N is defined as the sum of the weights.

As the wavelength range of our observations spans from 0.4 to 2.4 μm, we decide to perform for each observation two comparisons: one over the visible (VIS) wavelength range (0.4–1.0 μm) and one over the near-infrared (NIR) wavelength range (1.0–2.4 μm). The aim is to determine which wavelength range sets the strongest constraints on the various stellar parameters. When applied to observations, these separate studies will allow us to explore whether the parameters derived from optical and near-infrared wavelength using hydrostatic models are consistent with each other.

[2] In the empirical spectra, these regions are frequently affected by residual telluric absorption (even after correction). We set the weights to 0 in the following regions: 0.758–0.768 μm, 0.93–0.97 μm, 0.994–1.02 μm, 1.11–1.15 μm, 1.34–1.475 μm, 1.8–1.98 μm, 2.26–2.28 μm.

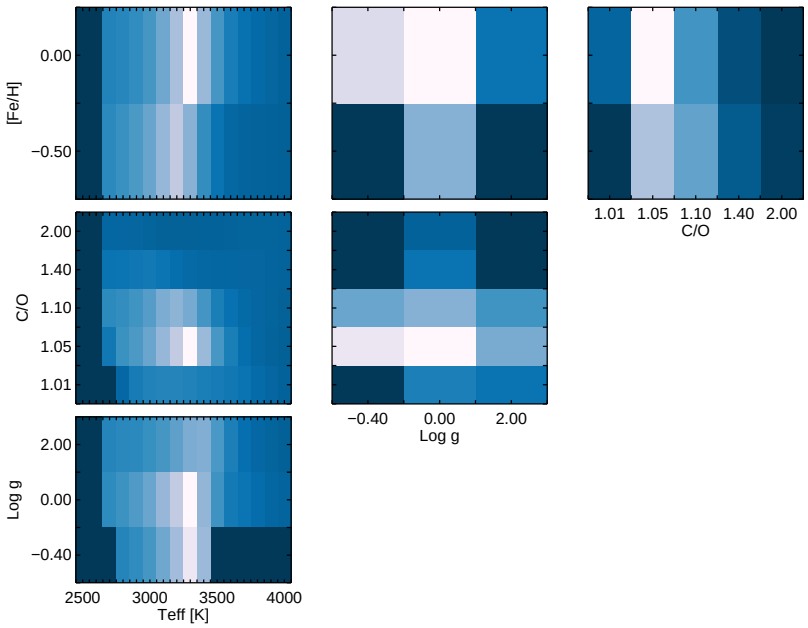

Figure 3.5: Example of χ^2 maps for one of our pseudo-observations ($T_{eff} = 3300$ K, $\log(g) = 0$, C/O = 1.05, [Fe/H] = 0) for the VIS wavelength range. The whiter colors stand for the lower χ^2 values.

3.4.3 χ^2 maps and results

For each pseudo-observation, we can compute a χ^2 map showing the distribution of the best models in the parameter space of the models. Figures 3.5 and 3.6 show an example of χ^2 maps for the fit of a pseudo-observation respectively over the VIS and NIR wavelength ranges. The best models, which correspond to the lowest value of the χ^2, are represented in white. The columns are from left to right: T_{eff}, $\log(g)$ and C/O. The rows are from bottom to top: $\log(g)$, C/O and [Fe/H]. The best values (i.e., the ones that minimize the χ^2 calculation) are represented in white.

In certain regimes, a degeneracy is seen between C/O and T_{eff} . The direction of the degeneracy depends on the wavelength range used. At NIR wavelengths, a higher estimated T_{eff} is associated with a higher estimated C/O ratio, while the opposite is found in the VIS (when the VIS shows any degeneracy).

Another more classical degeneracy is seen between [Fe/H] and T_{eff}: at higher T_{eff}, larger [Fe/H] are needed to produce strong features.

The peaked aspect of the maps shows that, within our limited grid of models, $\log(g)$ and [Fe/H] are relatively well constrained at all temperatures, the VIS constraints being significantly tighter than the NIR constraints. Of course, this may be different if the models are compared to real observations.

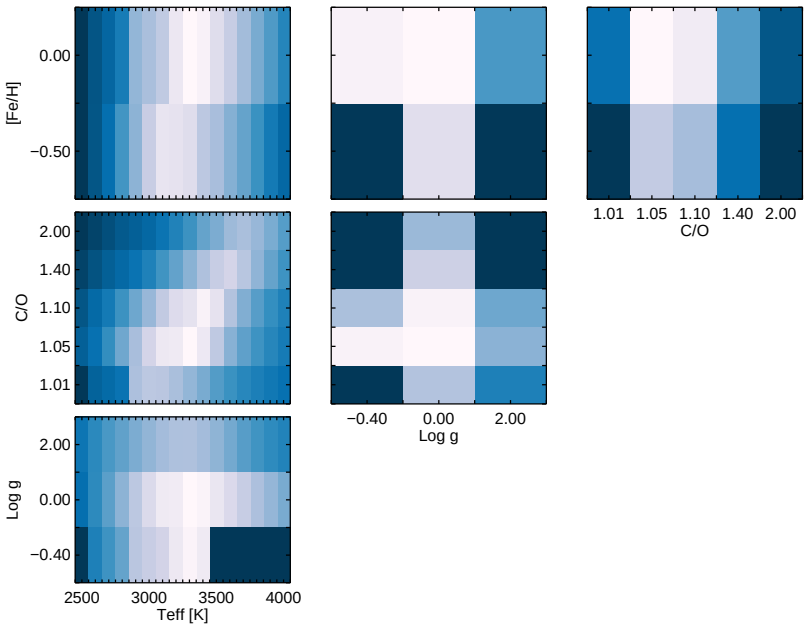

Figure 3.6: Example of χ^2 maps for one of our pseudo-observations (T_{eff} = 3300 K, log(g) = 0, C/O = 1.05, [Fe/H] = 0) for the NIR wavelength range. The whiter colors stand for the lower χ^2 values.

3.5 Comparison of observations and models

3.5.1 Color-color plot

We compute synthetic photometry through the 2MASS near-infrared filters (Cohen et al. 1992) and standard R and I filters (Bessell 1990). The results are displayed in Fig. 3.7 and in Appendix 3.42. The solid line in Fig. 3.7 shows the effect of a simple reddening screen (Cardelli et al. 1989). The colors of neither the reddest nor the bluest XSL spectra can be reproduced with the hydrostatic models and this extinction law.

A comparison of the colors of the XSL targets and those of models provides a sanity test on the energy distributions as well as information on effects of dust. At all but the lowest temperatures, color indices involving a near-infrared passband are good first order indicators of effective temperature, with a low sensitivity to other fundamental parameters. In that regime, only dust may have a strong effect on the colors.

The error bars are upper limits, as they are based on the dispersion in the distributions of differences between our photometry and the literature values (large amplitude variables excluded).

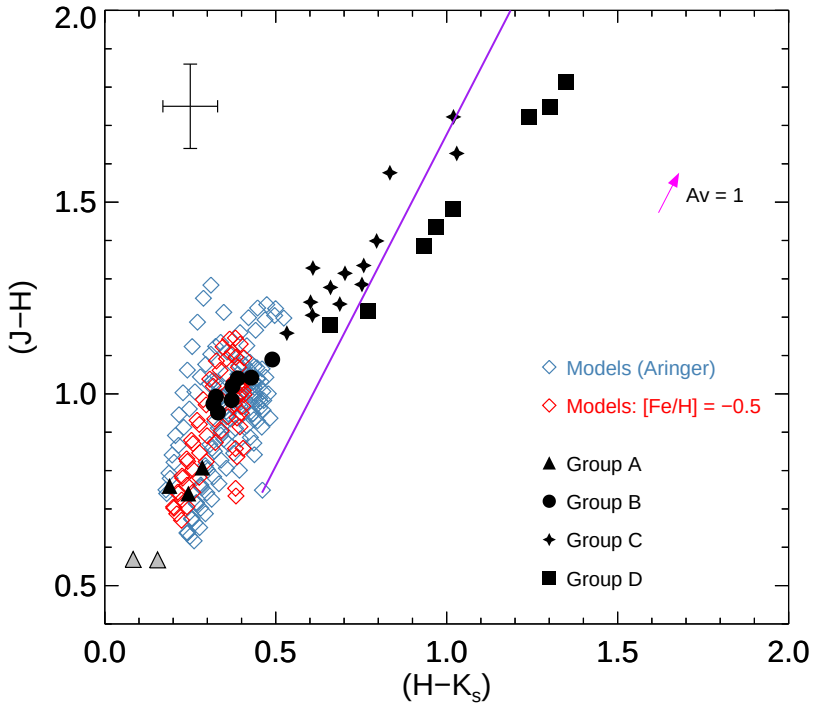

Figure 3.7: Colors (no correction for interstellar reddening) for our sample of carbon stars (filled symbols), using the 2MASS J, H and K_s filters. The synthetic colors (open diamonds) of our grid of hydrostatic models are overplotted for comparison. The plotted error bars are based on the dispersion in the distributions of differences between our photometry and the literature values (large amplitude variables excluded).

Group A gathers the bluest stars of our sample, represented as filled triangles in Figure 3.7. From this Figure, we clearly see that two of our stars, HD 202851 and HE 1428-1950, represented as grey triangles, are out of the parameter space of the models, and thus can not be reproduced with our current grid of models. Therefore, they are not considered in the comparison with the models.

Group D gathers all the stars with the absorption band at 1.53 μm (attributed to HCN+C_2H_2). Although a small number of hydrostatic models contains this feature, the current grid combined with simple extinction does not reach values of $(H - K_s)$ red enough to explain all the observations.

3.5.2 Molecular indices

Figure 3.8 shows the values of the spectroscopic indices designed for carbon stars in *Chapter 2*. In addition, we also plot the values for the $DIP153b$ index defined in Section 3.3.4. The filled symbols stand for our observations (the triangles are

for stars from Group A, the circles for Group B, the stars for Group C and the squares for Group D), while the open diamonds represent the models (in red we highlight the models with [Fe/H] = -0.5).

Error bars account for the noise per resolved element and uncertainties in the shape of the spectrograph's response curve in the scale of molecular features. The latter component is usually dominant because the signal-to-noise ratio of the spectra is of order 10^2. Uncertainties in the response curve on the relevant scales are due to a large part to imperfect modelling of the telluric absorption that affects spectro-photometric standard star observations.

Spectrophotometric indices provide a synthetic view of the models with respect to the XSL data, at a somewhat higher resolution than broad band colors. For brevity, we only discuss the loci in the bins of $(J-K_s)$, as already done in *Chapter 2*.

In general, the model loci agree well with the locus of the observations of our sample with $(J-K_s) < 1.8$. This is true in particular for the CN bands. The CO bands in the H window tend to be too strong in the models compared to the data. These features are sensitive to surface gravity at a given effective temperature. The relative strengths of the first and second overtone CO bands (measured by CO12 and COH) are also sensitive to the microturbulent velocity (Origlia et al. 1997; Lançon & Hauschildt 2010). It is as yet unclear what the predominant cause of the systematic difference should be. Like the data, the model indices present a large dispersion within color bins.

Some of the models display the 1.53 μm feature (panels d and g). However, these models do not display damped line forests in the H and K window, as seen in the corresponding observations (panes h and i). In *Chapter 2*, the damping of the high frequency structure in spectra with the 1.53 μm feature was interpreted as veiling by circumstellar dust. The index plots for the dust-free static models are consistent with this picture.

3.5.3 Full spectrum fits

For a direct comparison between the empirical and the model spectra, we use a methodology similar to Sect. 3.4.2. The differences are the following:

- The noise spectra of our observations are the ones that come out of the X-shooter reduction pipeline and we propagate them throughout all the reduction process, including the correction of the telluric features and the flux calibration.

- We degrade the resolution of the XSL spectra to $R \sim 2000$. The velocity resolution of the XSL data amounts $\sim$ 30 km/s. In Mira-type long period variables, velocity discontinuities with amplitudes larger than 10 km/s are expected as shocks propagate through the atmospheres (Nowotny et al. 2005). They produce significant wavelengths shifts that may differ for various molecular bands. We postpone the study of these high resolution effects to a future article.

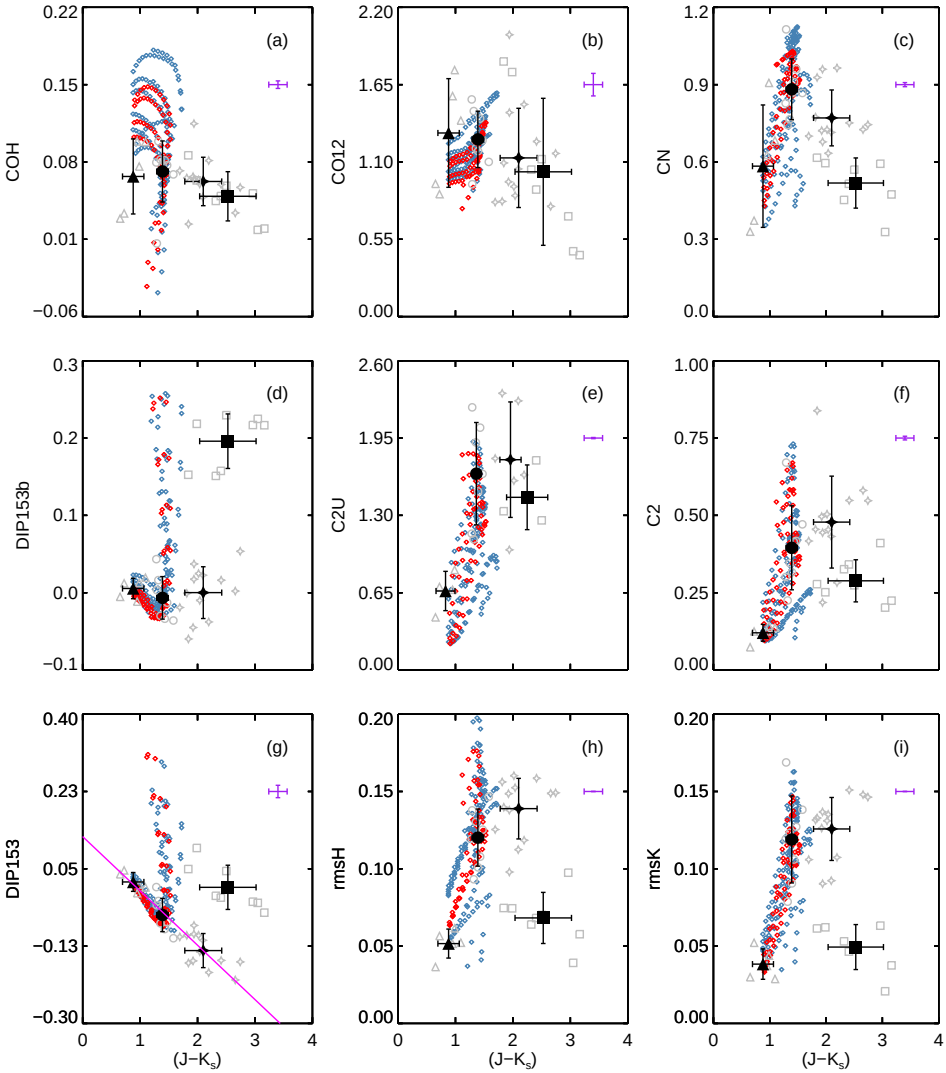

Figure 3.8: Some indices derived from our sample of carbon stars (black symbols) and the grid of models (color symbols) as a function of $(J - K_s)$. The triangles are for stars from Group A, the circles for Group B, the stars for Group C and the squares for Group D. The filled symbols represent the averaged values of our indices in the groups. The open diamonds represent the models at solar (in blue) and sub-solar metalliticity (red). The plotted error bars measure the dispersion within bins. The observational error bars are shown in purple.

3.5.4 Results

For each observation, the best model found is the one which minimizes the χ^2 calculation. We derive the range of acceptable parameters around the best models found over the VIS and the NIR wavelength ranges by setting the limit of χ^2/χ^2_{min} to 1.1.

Tables 3.3 to 3.6 show the range of values of the best models found while comparing our observations to the grid of models. The V letter indicates the values found over the VIS wavelength range, the N letter stands for near-infrared. As said before, what we call the visible wavelength range in this paper runs in principle from 0.4 μm to 1.0 μm, which covers in practice the UVB and VIS parts of X-shooter. But in practice, for some of the coolest stars, we do not have the full visible wavelength range. For each parameter (T_{eff}, log(g), C/O, [Fe/H]), the first column gives the value of the best model (i.e. the one that minimizes the χ^2 calculation), the second column gives the weighted best value and the third and fourth columns give the extreme values. The weighted value is calculated as follows:

$$param\_weighted = \frac{\sum_i param(i) \times exp(-(\chi^2_i/\chi^2_{min})/2)}{\sum_i exp(-(\chi^2_i/2 \times \chi^2_{min}))} \tag{3.3}$$

As a general comment for all our observations, the favoured surface gravity is log(g) = 0, and a metallicity of -0.5. These values are satisfactory for TP-AGB stars, and for a sample consisting mostly of LMC, SMC and Milky Way halo stars.

The best fits are shown in Appendix 3.A. For each observation, the upper panel shows the star spectrum as a black curve and the best model times the polynomial as a red curve. The weights applied for the χ^2 minimization are displayed in orange. The middle panel shows the residuals (in green), while the bottom panel shows the difference between the best model and a smoothed version of itself (in blue). In addition, a small insert shows the output χ^2/χ^2_{min} values as a function of the temperatures of the input models.

Figure 3.9 compares the values of the effective temperatures found while fitting the VIS and NIR wavelength range. The dashed line indicates the one-to-one relation. The symbols indicate the values for the different groups. The temperatures derived from our fits tend to be in general warmer in the VIS than in the NIR.

Group A The parameters listed in Table 3.3 agree quite well between the VIS and the NIR wavelength ranges. The best fits are shown from Figures 3.10 to 3.12. Effective temperatures in Group A are above 3750 K.

Two of the three stars in Group A display hydrogen lines in emission. They are large amplitude variables (*Chapter 2*) and the lines are interpreted as signatures of shocks that propagate through the atmosphere. For one of the stars, the model fit is not quite as good as for the others. But overall it is remarkable how well hydrostatic models reproduce the medium resolution spectral features of these warm pulsators.

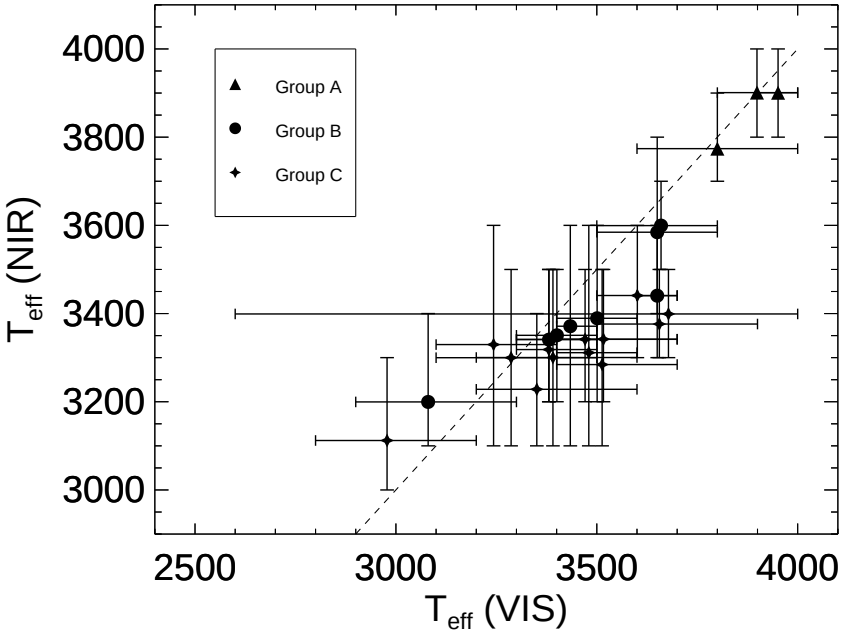

Figure 3.9: Comparison of the best values found for the effective temperature for both wavelength range (VIS and NIR), for Groups A, B and C. The dashed line indicates the one-to-one relation.

Group B Stars from Group B are the most likely to be reproduced by the grid of models, according to Fig. 3.7. The fits are good indeed, and the curves of χ^2 versus model T_{eff} are well behaved with narrow minima. The best values are summarized in Table 3.4. In all but one case (Fig. 3.14), the T_{eff} range derived from the VIS spectrum is narrower than the range accepted based on the NIR data, in agreement with expectations from Sec. 3.4. The temperatures within Group B are spread between 3100 and 3700 K.

In general, a slightly higher temperature in the VIS is compensated by a higher C/O ratio.

From Figures 3.13 to 3.20, some small discrepancies progressively appear. Some are probably instrumental, as the lack of data around 0.63 μm (due to a bad column). A real systematic difference in the shape and depth of the C_2 band at 1.77 μm becomes apparent for $(J - K) \geq 1.4$. This will be discussed further in Group C below.

Group C Table 3.5 summarizes the properties of the best models found for the stars of Group C. Stars from Group C are stars with $(J - K) \geq 1.6$ and they begin to be more affected by the pulsation than stars from the previous groups. Therefore, we are closer to the limits of what can be done with hydrostatic models. The best fits are shown from Figures 3.21 to 3.33.

The range of temperatures found in Group C is similar to that in Group B, despite the redder colors in Group C. The favour C/O value is 2. The effect of C/O on color, at a given T_{eff} (above 3000 K), is very small and hence C/O does not explain the redder colors of Group C. The difference in color between Groups B and C is mainly driven by circumstellar extinction.

Group D Table 3.6 summarizes the results for the stars from Group D, i.e the stars that display the 1.53 μm absorption feature. This subset is the one most affected by the effects of pulsation. It contains only large amplitude variables (cf. *Chapter 2*), and the use of hydrostatic models is a clear limitation. The fits are shown from Figures 3.34 to 3.41.

While the χ^2 distributions as a function of effective temperature remain relatively well behaved for most of the VIS spectra, the distributions for the NIR are very flat. A flat distribution means that the fits provide no or only weak constraints on the temperature. The NIR X-shooter spectra in Group D have a relatively smooth appearance, compared to Groups C and B, as was highlighted in *Chapter 2*. As a consequence, the best fit models tend to have relatively high temperatures (sometimes $>$ 3500 K), and they favour $\log(g)$=2 over $\log(g)$=0. Can we trust any of these? A hot temperature is difficult to reconcile with the presence of the 1.53 μm feature, and indeed high temperature fits fail to reproduce this (e.g. Fig. 3.40 and 3.41). A gravity as high as $\log(g)$=2 is difficult to reconcile with the expected location of large amplitude C-rich variables on the asymptotic giant branch. Our favoured interpretation is that these stars have normal AGB gravities and are not as warm as the NIR fits at $\log(g)$=2 may indicate. Instead, their spectra are profoundly modified by dust that produces both extinction and emission (the combination is known as veiling). The (additive) emission component attenuates the equivalent widths of molecular absorption features produced in the photosphere, and both extinction and emission affect the energy distribution. The parameters given in Table 3.6 based on the NIR spectra should not be relied on.

In principle, the parameters derived in the VIS should be more reliable than those based on the NIR, as dust emission is stronger at longer wavelengths and dust absorption does not modify molecular absorption equivalent widths. However, the useful part of the VIS spectrum of highly reddened objects contains almost exclusively signatures of CN, and one should keep in mind that unexplored parameters such as the Nitrogen abundance could affect these.

Finally, we emphasize two systematic spectral misfits. The C_2 feature at 1.77 μm is never matched correctly. And the 1.53 μm feature present in the coolest hydrostatic models does not have the shape of its observed counterpart (e.g. Fig. 3.35). The line lists for the main carriers (C_2 on one hand, HCN and C_2H_2 on the other) may need revision.

3.6 Conclusions

We have compared optical and near-infrared spectra of carbon stars with hydrostatic models at a spectral resolving power of $\sim$ 2000. The models provide impressive matches to most of the features in the optical and NIR range, but it remains difficult to fit all features simultaneously with a single model, when only extinction is allowed to alter the energy distribution.

In defining a goodness-of-fit criterion, choices can be made that focus either on the high frequency structure within the bands, or on the low resolution energy distribution. In this paper, we have emphasized the latter. XSL spectra contain a wealth of high frequency information, that will be exploited more completely in the future. A main difficulty encountered at the native resolution of the XSL data, R $\sim$ 10000 in the VIS and 8000 in the NIR, is an effect of pulsation. Shocks that travel through the atmospheres of Long Period Variables (LPV) create velocity discontinuities with amplitudes above 10 km/s, which will affect the location and shape of lines at the resolution of XSL. Smoothing to $R \sim 2000$ allows us to avoid this difficulty. Nevertheless, the residuals of the fits show that it remains difficult to fit all the spectral features even at low resolution, and even when a multiplicative polynomial mimicking extinction and flux calibration corrections is allowed to modify the energy distribution.

Quantitative criteria show it becomes progressively more difficult to obtain reasonable matches of the data for redder observed spectra. This is due to a combination of a more complex forest of molecular lines (that is only matched in detail in small parts of the spectra), and to the effects of circumstellar material on the energy distribution (that a simple extinction law cannot reproduce). Relaxing the assumptions on the energy distribution by allowing for an arbitrary polynomial in the fit will provide a complementary view on the respective roles of high and low resolution properties.

Effective temperature ranges derived from optical and NIR fits usually overlap when good fits are found, with a tendency for optical ranges to be narrower than NIR ranges. However, the ranges obtained with our current threshold are very broad.

The fits show that the R $\sim$ 2000 features in the models are not perfect representations of the data. This justifies the use of empirical spectra as templates for C stars in the universe. At this stage however, it is not possible to assign an evolutionary stage precisely to individual stars in the collection based on their spectra alone. When using the C-star observations as templates, it will probably be necessary to continue to use averages, as done for instance by Lançon & Mouhcine (2002) for O-rich and C-rich LPVs.

Appendix 3.A Comparison observations - mo-dels: best fits

Tables 3.3 to 3.6 show the range of parameters of the best models. Figures 3.10 to 3.41 show the best fits of our observations. For each figure, the upper panel shows the observation (black curve), the best model times the polynomial (red

curve) and the weights used for the χ^2 minimization (orange). The middle panel shows the residuals (in green), while the bottom panel shows the difference between the best model and a smoothed version of itself (in blue).

		T_{eff}				log(g)				C/O				[Fe/H]			
Name	Waves	Best	Wei	Min	Max	Best	Wei	Min	Max	Best	Wei	Min	Max	Best	Wei	Min	Max
Cl* NGC 121 T V8	V	4000	3951	3900	4000	0.0	0.0	0.0	0.0	1.40	1.40	1.40	1.40	−0.5	−0.5	−0.5	−0.5
	N	3900	3900	3800	4000	0.0	0.3	0.0	2.0	1.10	1.13	1.05	1.40	−0.5	−0.4	−0.5	0.0
SHV 0518161−683543	V	3900	3800	3600	4000	0.0	0.0	0.0	0.0	1.40	1.28	1.10	1.40	−0.5	−0.5	−0.5	−0.5
	N	3700	3773	3700	3900	0.0	0.0	0.0	0.0	1.10	1.16	1.05	1.40	−0.5	−0.5	−0.5	−0.5
SHV 0517337−725738	V	3800	3898	3800	4000	0.0	0.0	0.0	0.0	1.40	1.60	1.40	2.00	−0.5	−0.5	−0.5	−0.5
	N	4000	3900	3800	4000	0.0	0.0	0.0	0.0	1.40	1.30	1.10	1.40	−0.5	−0.5	−0.5	−0.5

Table 3.3: Range of parameters for the best fits for the stars from Group A

		T_{eff}				log(g)				C/O				[Fe/H]			
Name	Waves	Best	Wei	Min	Max	Best	Wei	Min	Max	Best	Wei	Min	Max	Best	Wei	Min	Max
2MASS J00571648-7310527	V	3700	3650	3600	3700	0.0	0.0	0.0	0.0	2.00	1.70	1.40	2.00	−0.5	−0.5	−0.5	−0.5
	N	3400	3440	3300	3600	0.0	0.8	0.0	2.0	1.10	1.13	1.05	1.40	−0.5	−0.3	−0.5	0.0
2MASS J00563906-7304529	V	3100	3080	2900	3300	−0.4	−0.1	−0.4	0.0	1.10	1.24	1.05	1.40	0.0	−0.1	−0.5	0.0
	N	3200	3199	3100	3400	0.0	0.0	0.0	0.0	2.00	1.78	1.40	2.00	−0.5	−0.2	−0.5	0.0
2MASS J01003150-7307237	V	3700	3650	3500	3800	0.0	0.0	0.0	0.0	1.40	1.39	1.05	2.00	−0.5	−0.5	−0.5	−0.5
	N	3600	3584	3400	3800	0.0	0.0	0.0	0.0	1.10	1.18	1.05	1.40	−0.5	−0.5	−0.5	−0.5
2MASS J00530765−7307477	V	3600	3659	3500	3800	0.0	0.0	0.0	0.0	2.00	2.00	2.00	2.00	−0.5	−0.3	−0.5	0.0
	N	3600	3599	3500	3700	0.0	0.0	0.0	0.0	2.00	1.80	1.40	2.00	−0.5	−0.5	−0.5	−0.5
2MASS J00493262-7317523	V	3500	3500	3400	3600	0.0	0.0	0.0	0.0	1.40	1.60	1.40	2.00	−0.5	−0.5	−0.5	−0.5
	N	3400	3389	3200	3600	0.0	0.7	0.0	2.0	1.10	1.14	1.05	1.40	−0.5	−0.3	−0.5	0.0
2MASS J00490032-7322238	V	3500	3434	3400	3500	0.0	0.0	0.0	0.0	2.00	1.80	1.40	2.00	−0.5	−0.5	−0.5	−0.5
	N	3400	3371	3100	3600	0.0	0.0	0.0	0.0	1.40	1.44	1.10	2.00	−0.5	−0.5	−0.5	−0.5
2MASS J00571214-7307045	V	3500	3400	3300	3500	0.0	0.0	0.0	0.0	2.00	1.70	1.40	2.00	−0.5	−0.5	−0.5	−0.5
	N	3400	3350	3200	3500	0.0	0.0	0.0	0.0	1.40	1.48	1.10	2.00	−0.5	−0.5	−0.5	−0.5
2MASS J00570070-7307505	V	3400	3381	3300	3500	0.0	0.0	0.0	0.0	2.00	1.77	1.40	2.00	−0.5	−0.5	−0.5	−0.5
	N	3400	3340	3200	3500	0.0	0.0	0.0	0.0	2.00	1.76	1.40	2.00	−0.5	−0.5	−0.5	−0.5

Table 3.4: Range of parameters for the best fits for the stars from Group B

		T_{eff}				log(g)				C/O				[Fe/H]			
Name	Waves	Best	Wei	Min	Max	Best	Wei	Min	Max	Best	Wei	Min	Max	Best	Wei	Min	Max
2MASS J00564478-7314347	V	3600	3600	3500	3700	0.0	0.0	0.0	0.0	2.00	2.00	2.00	2.00	−0.5	−0.5	−0.5	−0.5
	N	3500	3440	3300	3600	0.0	0.0	0.0	0.0	2.00	1.76	1.40	2.00	−0.5	−0.5	−0.5	−0.5
2MASS J00542265-7301057	V	3500	3516	3400	3700	0.0	0.0	0.0	0.0	2.00	1.80	1.40	2.00	−0.5	−0.5	−0.5	−0.5
	N	3400	3341	3200	3500	0.0	0.0	0.0	0.0	2.00	1.76	1.40	2.00	−0.5	−0.5	−0.5	−0.5
IRAS 09484-6242	V	3000	2977	2800	3200	0.0	0.0	0.0	0.0	2.00	1.74	1.40	2.00	−0.5	−0.5	−0.5	−0.5
	N	3100	3112	3000	3300	0.0	0.0	0.0	0.0	2.00	1.93	1.40	2.00	−0.5	−0.2	−0.5	0.0
Cl* NGC 419 LE 27	V	3600	3470	3300	3700	0.0	0.0	0.0	0.0	2.00	1.55	1.05	2.00	−0.5	−0.5	−0.5	−0.5
	N	3400	3341	3200	3500	0.0	0.0	0.0	0.0	2.00	1.77	1.40	2.00	−0.5	−0.5	−0.5	−0.5
[W65] c2	V	3900	3678	2600	4000	0.0	0.2	0.0	2.0	2.00	1.70	1.10	2.00	−0.5	−0.4	−0.5	0.0
	N	3400	3399	3300	3500	0.0	0.0	0.0	0.0	1.05	1.07	1.05	1.10	−0.5	−0.5	−0.5	−0.5
SHV 0520427-693637	V	3500	3480	3400	3600	0.0	0.0	0.0	0.0	2.00	1.76	1.40	2.00	−0.5	−0.5	−0.5	−0.5
	N	3200	3311	3100	3600	2.0	0.9	0.0	2.0	1.10	1.46	1.05	2.00	0.0	−0.3	−0.5	0.0
2MASS J00553091-7310186	V	3600	3513	3400	3700	0.0	0.0	0.0	0.0	2.00	1.67	1.10	2.00	−0.5	−0.5	−0.5	−0.5
	N	3300	3284	3100	3500	0.0	0.0	0.0	0.0	2.00	1.80	1.40	2.00	−0.5	−0.5	−0.5	−0.5
Cl* NGC 419 LE 35	V	3800	3655	3500	3900	0.0	0.4	0.0	2.0	2.00	1.42	1.05	2.00	−0.5	−0.4	−0.5	0.0
	N	3400	3376	3300	3500	0.0	0.0	0.0	0.0	2.00	1.85	1.40	2.00	−0.5	−0.5	−0.5	−0.5
SHV 0504353−712622	V	3400	3380	3300	3500	0.0	0.0	0.0	0.0	2.00	1.76	1.40	2.00	−0.5	−0.5	−0.5	−0.5
	N	3500	3318	3200	3500	0.0	0.3	0.0	2.0	2.00	1.65	1.10	2.00	−0.5	−0.4	−0.5	0.0
T Cae	V	3300	3243	3100	3400	0.0	0.0	0.0	0.0	1.40	1.23	1.10	1.40	−0.5	−0.3	−0.5	0.0
	N	3300	3329	3100	3600	0.0	0.4	0.0	2.0	1.10	1.13	1.05	1.40	−0.5	−0.4	−0.5	0.0
[ABC89] Cir 18	V	3500	3350	3200	3600	0.0	0.2	0.0	2.0	2.00	1.47	1.05	2.00	−0.5	−0.5	−0.5	0.0
	N	3200	3228	3100	3400	0.0	0.0	0.0	0.0	2.00	1.83	1.40	2.00	−0.5	−0.4	−0.5	0.0
[ABC89] Pup 42	V	3500	3390	3200	3600	0.0	0.0	0.0	0.0	2.00	1.45	1.05	2.00	−0.5	−0.5	−0.5	−0.5
	N	3300	3300	3100	3500	0.0	0.0	0.0	0.0	2.00	1.80	1.40	2.00	−0.5	−0.4	−0.5	0.0
[ABC89] Cir 18	V	3400	3286	3100	3500	0.0	0.1	0.0	2.0	2.00	1.37	1.05	2.00	−0.5	−0.5	−0.5	0.0
	N	3300	3299	3100	3500	0.0	0.0	0.0	0.0	2.00	1.78	1.40	2.00	−0.5	−0.4	−0.5	0.0

Table 3.5: Range of parameters for the best fits for the stars from Group C

		T_{eff}				log(g)				C/O				[Fe/H]			
Name	Waves	Best	Wei	Min	Max	Best	Wei	Min	Max	Best	Wei	Min	Max	Best	Wei	Min	Max
SHV 0500412-684054	V	3600	3550	3500	3600	0.0	0.0	0.0	0.0	2.00	1.70	1.40	2.00	−0.5	−0.5	−0.5	−0.5
	N	3400	3407	2700	3800	2.0	1.1	0.0	2.0	1.05	1.33	1.05	2.00	0.0	−0.2	−0.5	0.0
SHV 0502469-692418	V	3300	3349	3200	3500	0.0	0.0	0.0	0.0	1.10	1.18	1.05	1.40	−0.5	−0.5	−0.5	−0.5
	N	2700	–	–	–	2.0	–	–	–	1.05	–	–	–	0.0	–	–	–
SHV 0527072-701238	V	3500	3658	3500	3800	2.0	0.8	0.0	2.0	1.05	1.50	1.05	2.00	0.0	−0.3	−0.5	0.0
	N	3500	3380	2700	4000	2.0	1.3	0.0	2.0	1.05	1.37	1.05	2.00	0.0	−0.2	−0.5	0.0
SHV 0520505-705019	V	3700	3699	3600	3800	0.0	0.0	0.0	0.0	2.00	2.00	2.00	2.00	−0.5	−0.5	−0.5	−0.5
	N	3300	3326	3000	3700	2.0	1.5	0.0	2.0	1.05	1.26	1.05	2.00	0.0	−0.1	−0.5	0.0
SHV 0518222-750327	V	3600	3599	3500	3700	0.0	0.0	0.0	0.0	2.00	1.70	1.40	2.00	−0.5	−0.5	−0.5	−0.5
	N	3400	3422	3000	3800	2.0	1.2	0.0	2.0	1.05	1.33	1.05	2.00	0.0	−0.2	−0.5	0.0
SHV 0536139-701604	V	3500	3614	3400	3900	2.0	0.4	0.0	2.0	1.05	1.41	1.05	2.00	0.0	−0.4	−0.5	0.0
	N	3200	3246	3000	3600	2.0	0.9	0.0	2.0	1.10	1.41	1.05	2.00	0.0	−0.3	−0.5	0.0
SHV 0525478-690944	V	3800	3808	3500	4000	2.0	1.5	0.0	2.0	1.05	1.15	1.01	2.00	0.0	−0.1	−0.5	0.0
	N	4000	3802	3600	4000	0.0	0.8	0.0	2.0	2.00	1.63	1.05	2.00	−0.5	−0.3	−0.5	0.0
SHV 0528537-695119	V	4000	3883	3700	4000	0.0	0.7	0.0	2.0	2.00	1.49	1.05	2.00	−0.5	−0.3	−0.5	0.0
	N	3900	3700	3400	4000	0.0	0.9	0.0	2.0	2.00	1.51	1.05	2.00	−0.5	−0.3	−0.5	0.0

Table 3.6: Range of parameters for the best fits for the stars from Group D

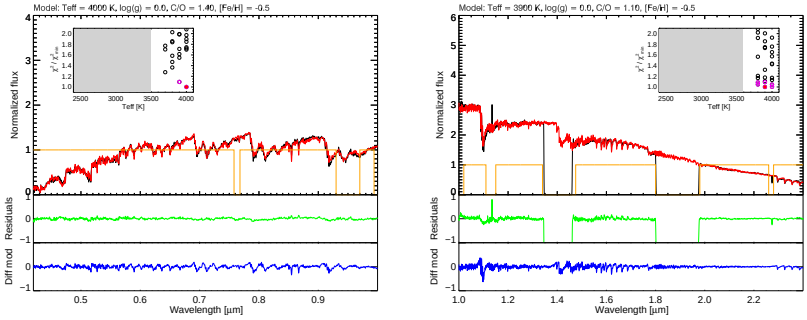

(a) VIS **(b)** NIR

Figure 3.10: Best fit for Cl* NGC 121 T V8 (Group A).

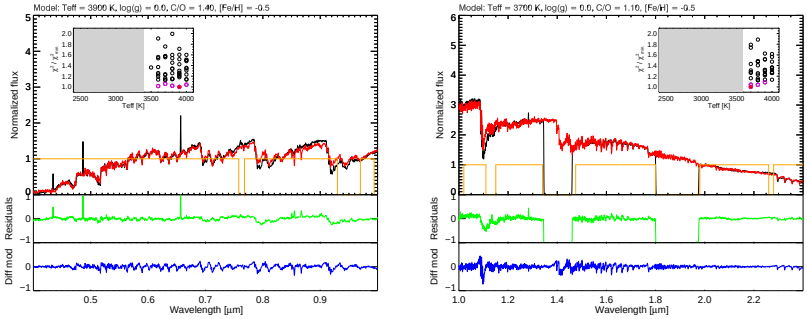

(a) VIS **(b)** NIR

Figure 3.11: Best fit for SHV 0518161-683543 (Group A).

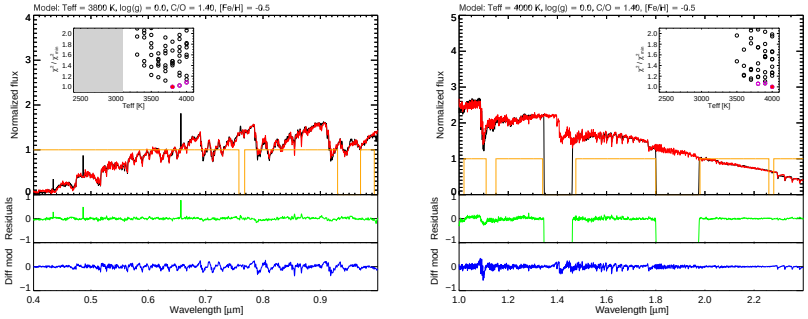

(a) VIS **(b)** NIR

Figure 3.12: Best fit for SHV 0517337-725738 (Group A).

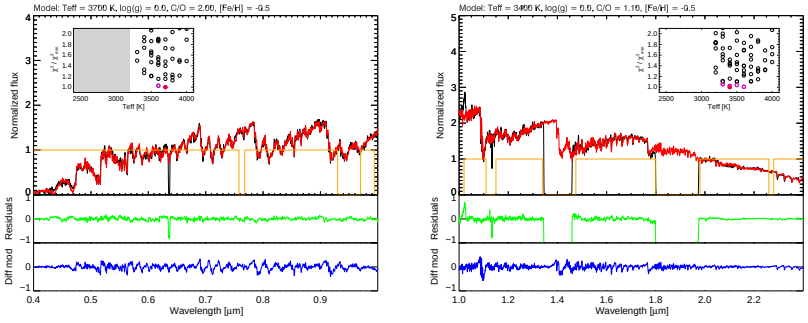

(a) VIS **(b)** NIR

Figure 3.13: Best fit for 2MASS J00571648-7310527 (Group B).

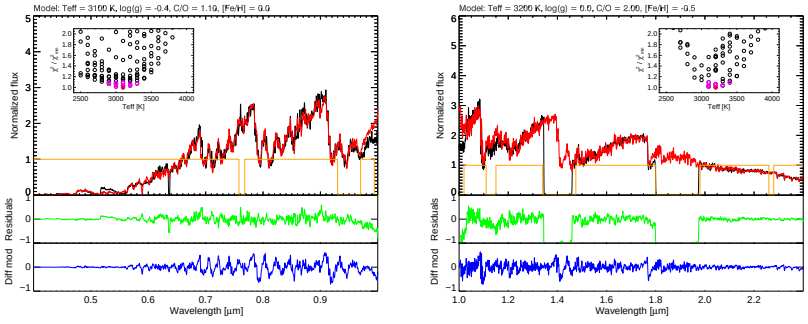

(a) VIS **(b)** NIR

Figure 3.14: Best fit for 2MASS J00563906-7304529 (Group B).

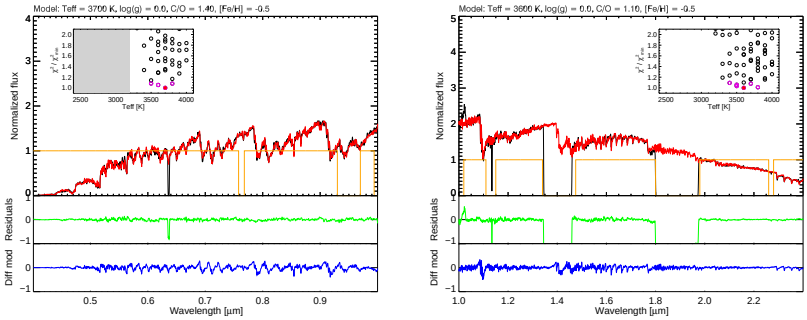

(a) VIS **(b)** NIR

Figure 3.15: Best fit for 2MASS J01003150-7307237 (Group B).

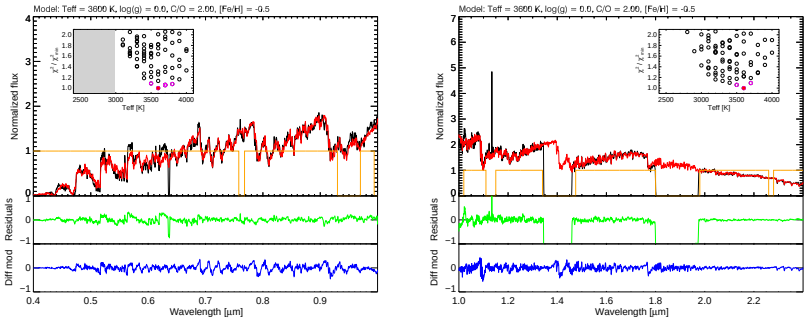

(a) VIS **(b)** NIR

Figure 3.16: Best fit for 2MASS J00530765-7307477 (Group B).

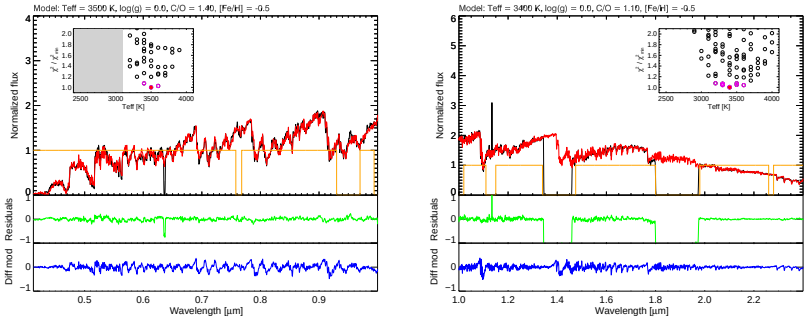

(a) VIS **(b)** NIR

Figure 3.17: Best fit for 2MASS J00493262-7317523 (Group B).

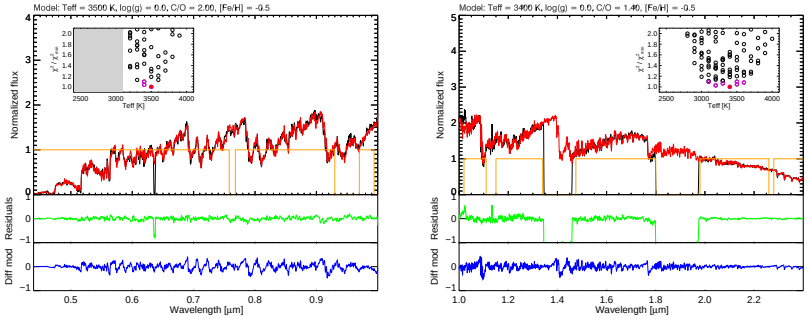

(a) VIS **(b)** NIR

Figure 3.18: Best fit for 2MASS J00490032-7322238 (Group B).

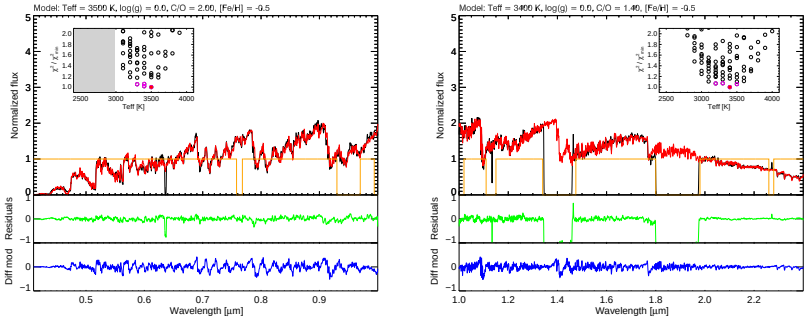

(a) VIS **(b)** NIR

Figure 3.19: Best fit for 2MASS J00571214-7307045 (Group B).

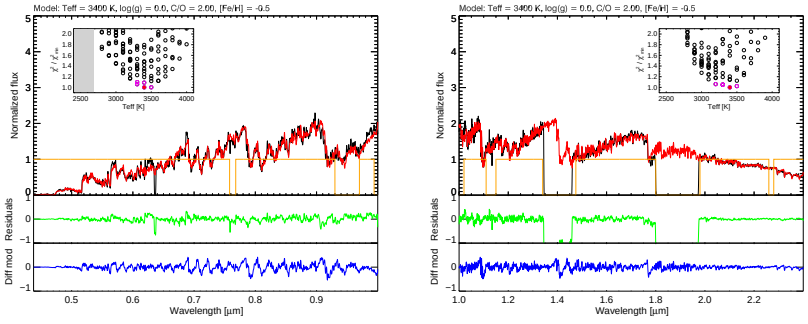

(a) VIS **(b)** NIR

Figure 3.20: Best fit for 2MASS J00570070-7307505 (Group B).

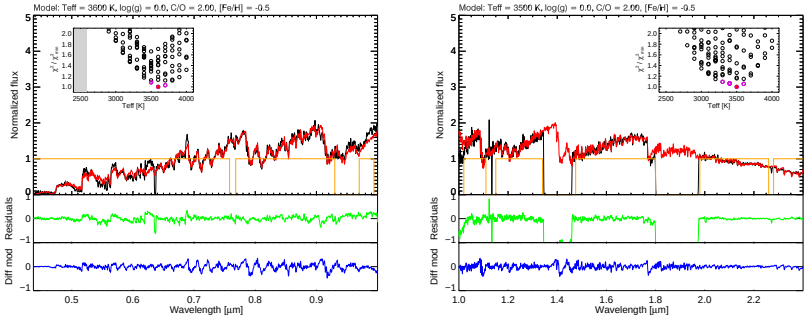

(a) VIS **(b)** NIR

Figure 3.21: Best fit for 2MASS J00564478-7314347 (Group C).

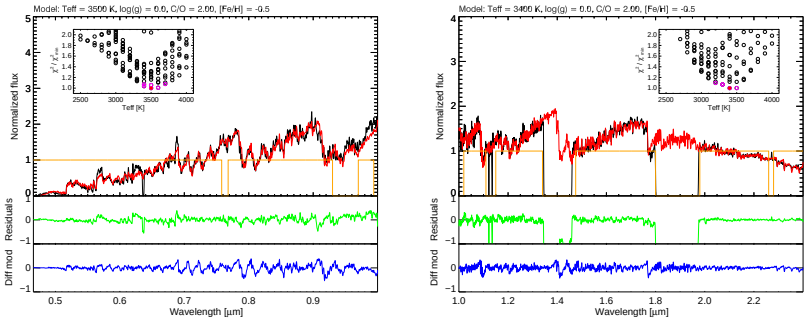

(a) VIS **(b)** NIR

Figure 3.22: Best fit for 2MASS J00542265-7301057 (Group C).

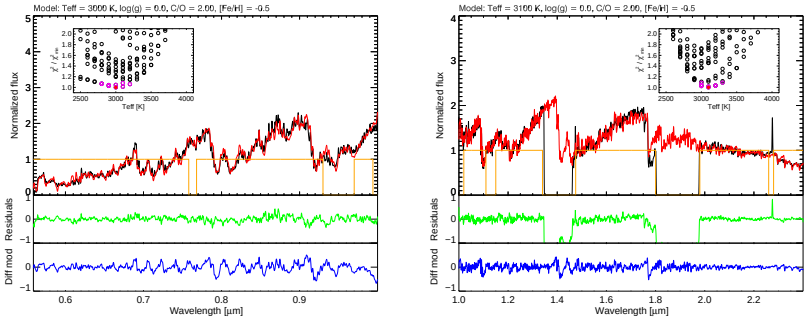

(a) VIS **(b)** NIR

Figure 3.23: Best fit for IRAS 09484-6242 (Group C).

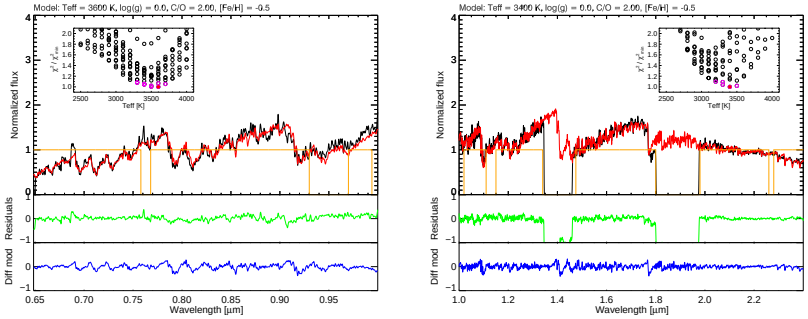

(a) VIS **(b)** NIR

Figure 3.24: Best fit for Cl* NGC 419 LE 27 (Group C).

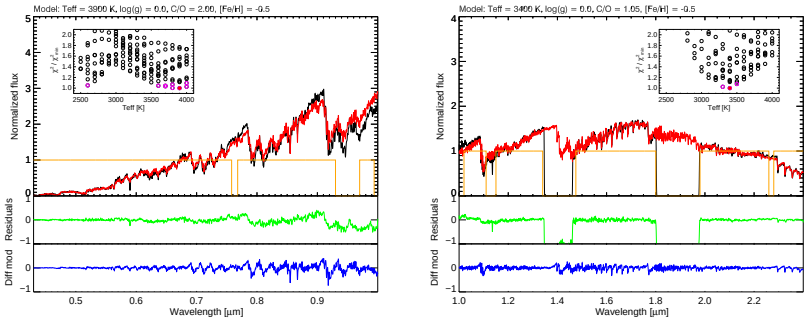

(a) VIS **(b)** NIR

Figure 3.25: Best fit for [W65] c2 (Group C).

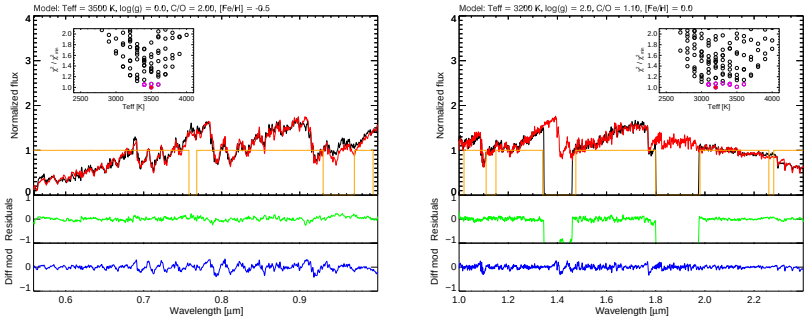

(a) VIS **(b)** NIR

Figure 3.26: Best fit for SHV 0520427-693637 (Group C).

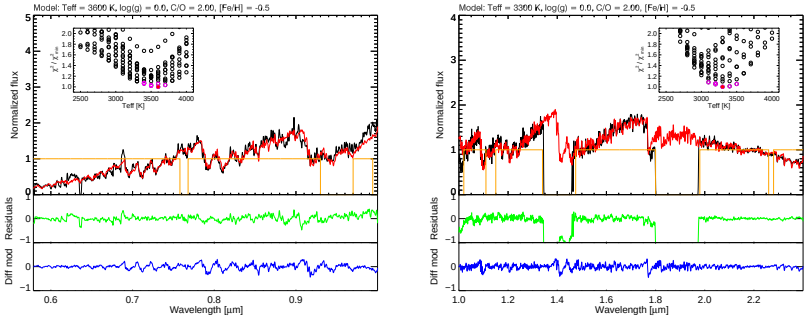

(a) VIS **(b)** NIR

Figure 3.27: Best fit for 2MASS J00553091-7310186 (Group C).

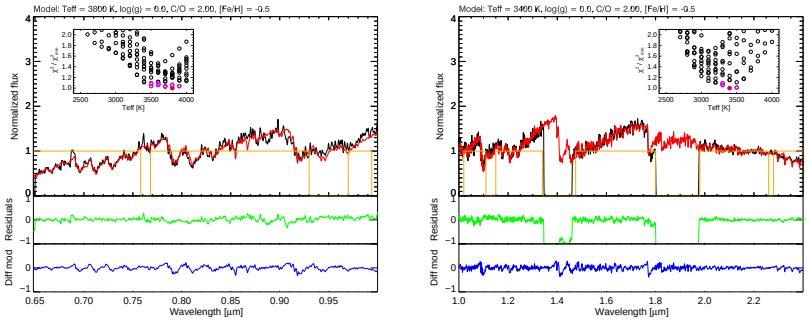

(a) VIS **(b)** NIR

Figure 3.28: Best fit for Cl* NGC 419 LE 35 (Group C).

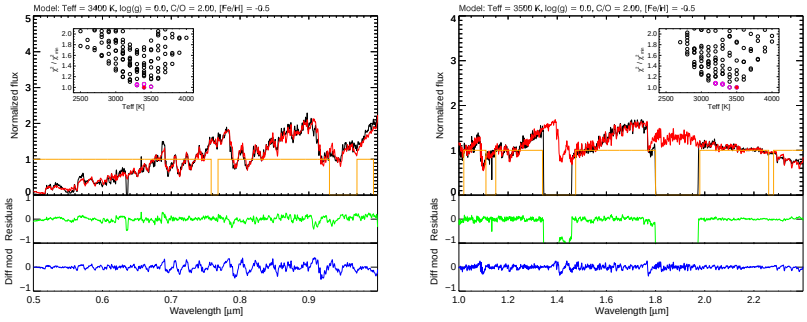

(a) VIS **(b)** NIR

Figure 3.29: Best fit for SHV 0504353-712622 (Group C).

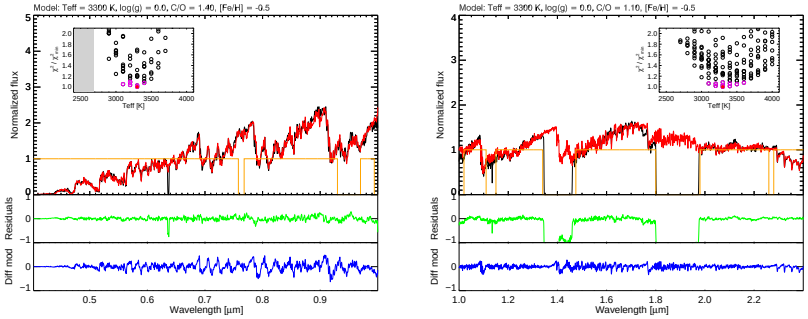

(a) VIS **(b)** NIR

Figure 3.30: Best fit for T Cae (Group C).

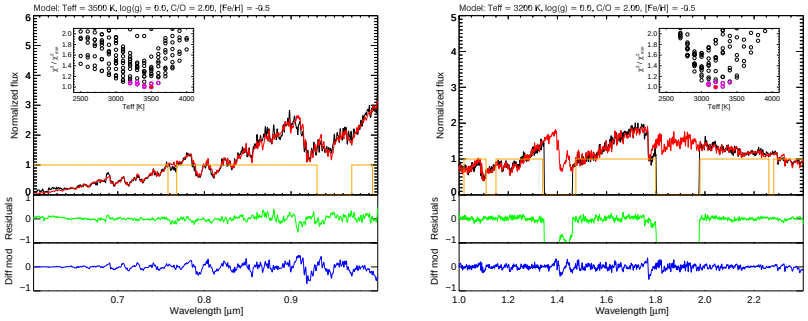

(a) VIS **(b)** NIR

Figure 3.31: Best fit for [ABC89] Cir 18 (Group C).

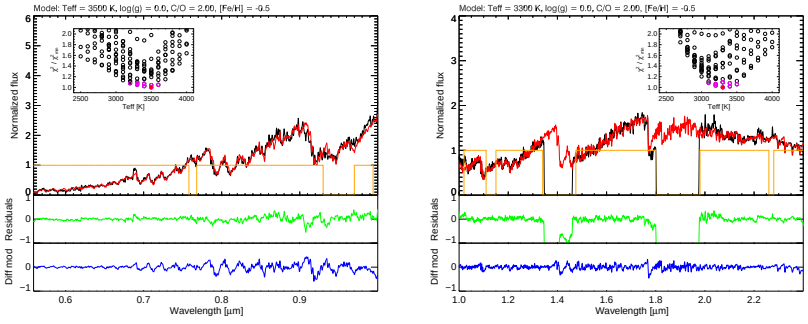

(a) VIS **(b)** NIR

Figure 3.32: Best fit for [ABC89] Pup 42 (Group C).

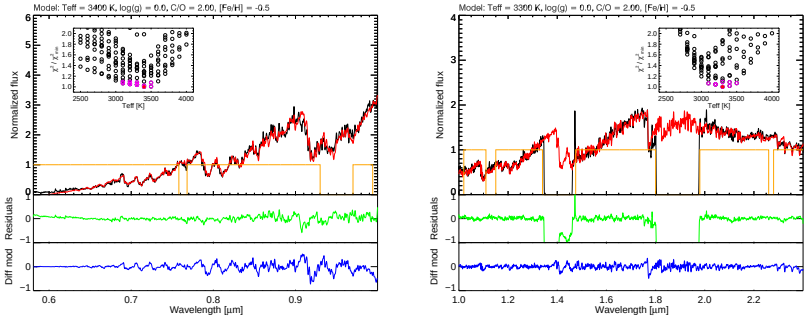

(a) VIS **(b)** NIR

Figure 3.33: Best fit for [ABC89] Cir 18 (Group C).

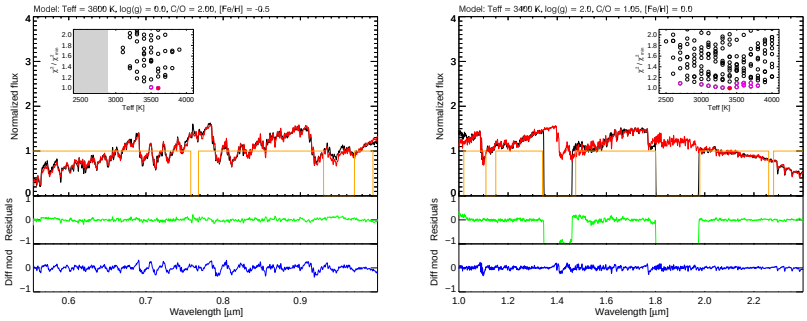

(a) VIS **(b)** NIR

Figure 3.34: Best fit for SHV 0500412-684054 (Group D).

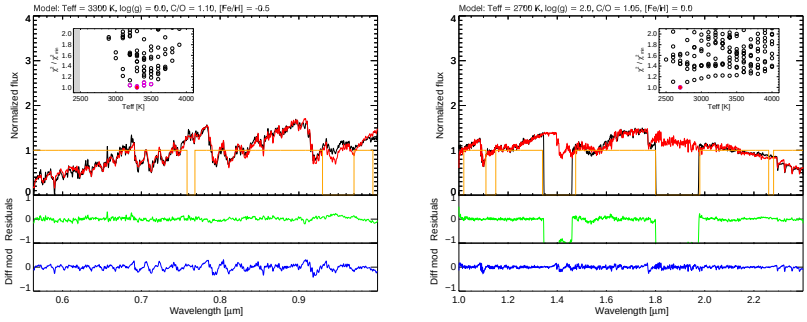

(a) VIS **(b)** NIR

Figure 3.35: Best fit for SHV 0502469-692418 (Group D).

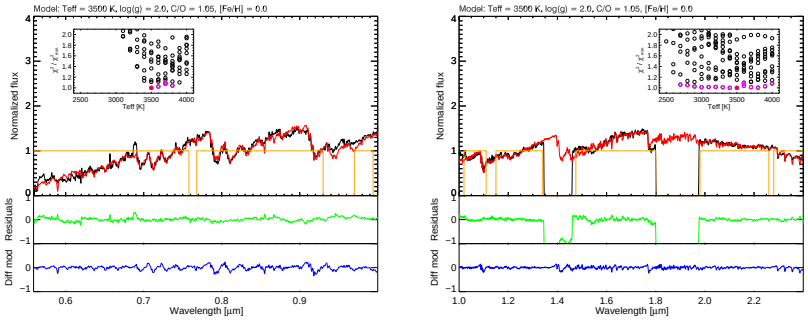

(a) VIS **(b)** NIR

Figure 3.36: Best fit for SHV 0527072-701238 (Group D).

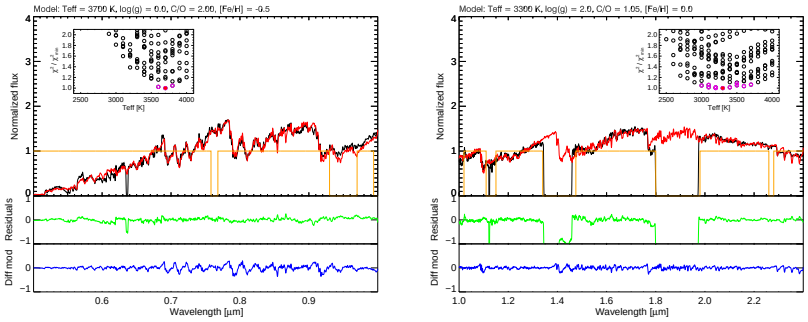

(a) VIS **(b)** NIR

Figure 3.37: Best fit for SHV 0520505-705019 (Group D).

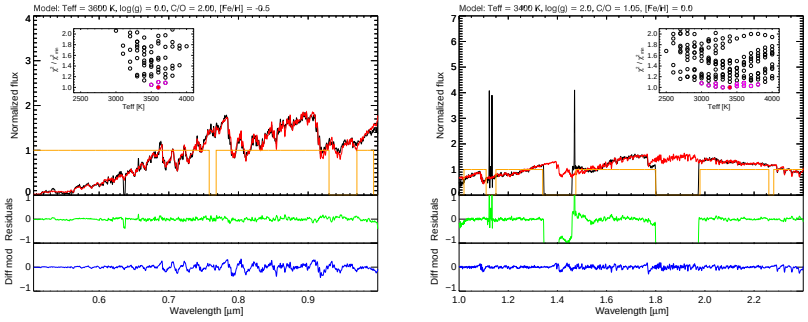

(a) VIS **(b)** NIR

Figure 3.38: Best fit for SHV 0518222-750327 (Group D).

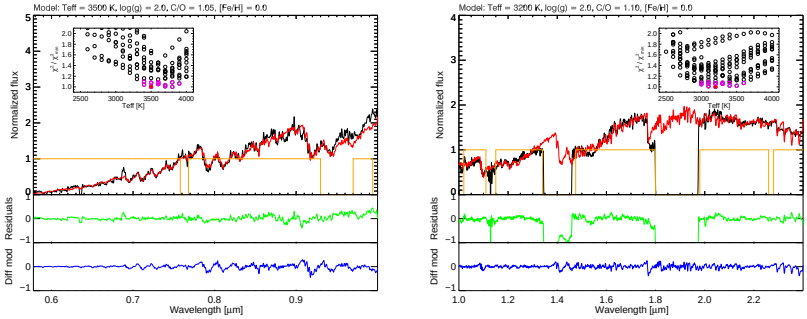

(a) VIS **(b)** NIR

Figure 3.39: Best fit for SHV 0536139-701604 (Group D).

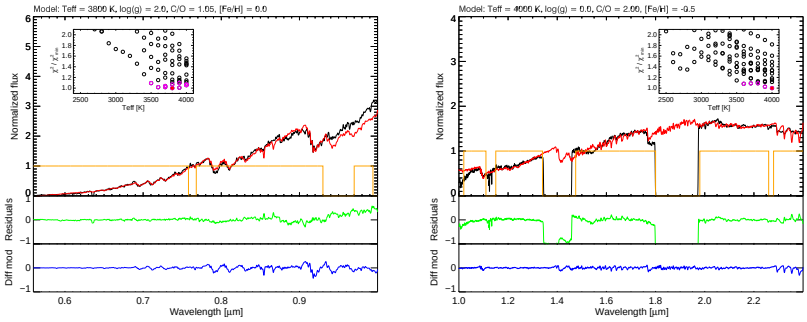

(a) VIS **(b)** NIR

Figure 3.40: Best fit for SHV 0525478-690944 (Group D).

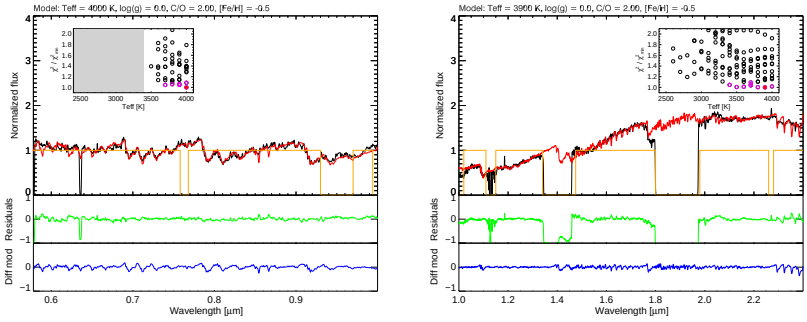

(a) VIS **(b)** NIR

Figure 3.41: Best fit for SHV 0528537-695119 (Group D).

Appendix 3.B Color-color plots

Figure 3.42 shows the color-color plot for our observations and the grid of models.

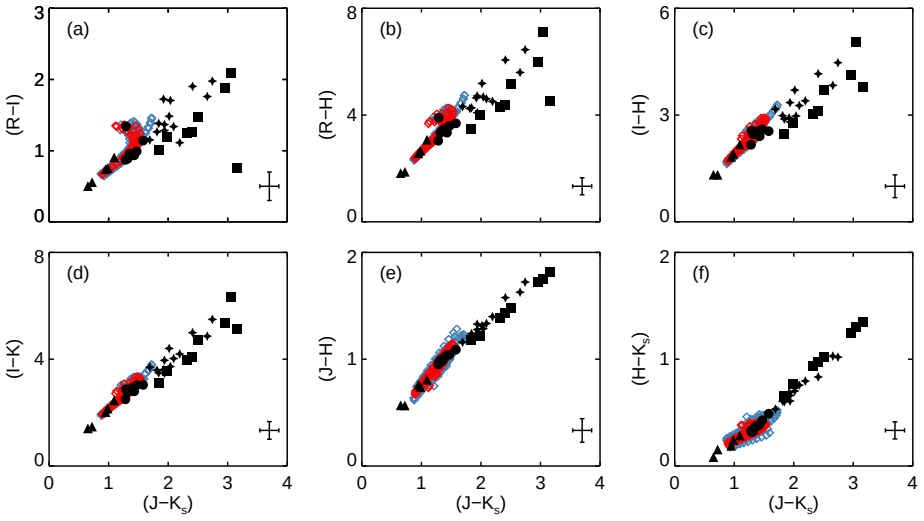

Figure 3.42: Some color-color plots derived from our sample of carbon stars (filled symbols) and the models (open diamonds). The triangles are for stars from Group A, the circles for Group B, the stars for Group C and the squares for Group D. The open diamonds represent the models at solar (in blue) and sub-solar metalliticity (red). The plotted error bars are upper limits, as they are based on the dispersion in the distributions of differences between our photometry and the literature (large amplitude variables excluded).